THE ASTROPHYSICAL JOURNAL, 345:584–596, 1989 October 1

TWO-DIMENSIONAL MAGNETOHYDRODYNAMIC MODEL OF EMERGING MAGNETIC FLUX IN THE SOLAR ATMOSPHERE

K. SHIBATA,[1] T. TAJIMA, AND R. S. STEINOLFSON
Department of Physics and Institute for Fusion Studies, University of Texas, Austin

AND

R. MATSUMOTO
Department of Information Science, College of Arts and Sciences, Chiba University, Chiba, Japan
Received 1988 August 25; accepted 1989 February 24

ABSTRACT

A two-dimensional magnetohydrodynamic code is used to study the nonlinear evolution of the undular mode of the magnetic buoyancy instability (the Parker instability) in an isolated horizontal magnetic flux embedded in a two-temperature layered atmosphere (solar corona–chromosphere/photosphere). The numerical results are analyzed in detail and compared with observed data for emerging magnetic flux in the solar atmosphere. The flux sheet with $\beta \simeq 1$ is initially located at the bottom of the photosphere. As the instability develops, the gas slides down the expanding loop, and the evacuated loop rises as a result of enhanced magnetic buoyancy. This expanding magnetic flux is identified as the emerging magnetic flux. In the nonlinear regime of the instability, the expansion of the magnetic loop (arch) shows self-similar behavior: the rise velocity of a magnetic loop and the local Alfvén speed at the top of the loop increase linearly with height as long as the magnetic pressure of the loop is larger than the coronal total pressure. The rise velocity of the magnetic loop in the high chromosphere ($h \simeq$ 4000–6000 km) is 10–15 km s^{-1}, and the velocity of downflow along the loop is 30–50 km s^{-1}, both of which are consistent with observed values for arch filament systems. Numerical results also explain the small rise velocity of emerging magnetic flux in the photosphere, and strong downdrafts near photospheric pores. The effects of interaction and reconnection with overlying magnetic fields in the network or in a preexisting active region are also investigated.

Subject headings: hydromagnetics — instabilities — plasmas — Sun: atmosphere — Sun: magnetic fields

I. INTRODUCTION

It is now well established that sunspots and active regions are formed by the emergence of magnetic flux tubes from the interior of the Sun into the solar atmosphere (e.g., Zwaan 1985, 1987). The newly emerged bipolar active regions are called emerging flux regions (EFRs; Zirin 1970, 1972). There are several observational evidences which indicate the emergence and rising motion of magnetic flux tubes in the EFR. Bruzek (1967, 1969) found from Hα observations that the loops (or filaments) with a length of about 10^4 km rise through the upper chromosphere with a speed of 10–15 km s^{-1} associated with the birth of sunspots. He also observed downflows of about 50 km s^{-1} along rising filaments, and interpreted these downflows as the sliding motion of gas along the rising loop due to gravity. (Chou and Zirin 1988 and Suematsu 1987 confirmed the above dynamical features and studied them in more detail using newer instruments.) Bruzek called the whole system the arch filament system (AFS). The AFS lasts for a few days in the case of an EFR that develops into bipolar spots with penumbrae (Weart 1970; Frazier 1972; Zirin 1974). However, few of the short-lived and small-scale ephemeral regions form an AFS (Harvey and Martin 1973).

Other interesting characteristics of EFR or AFSs are enhanced activities associated with them, such as bright plages observed near the footpoints of the loops (Bumba and Howard 1965; Born 1974; Glackin 1975; Kawaguchi and Kitai 1976; Zwaan 1987). Some X-ray bright points (XBPs) with a size of a few times 10^4 km are identified as EFRs or ephemeral regions (Harvey, Harvey, and Martin 1975; Golub, Krieger, and Vaiana 1976; Golub *et al.* 1977; Sheeley and Golub 1979). Surges or small flares are sometimes observed in EFRs (Marsh 1978; Kurokawa 1988*a*), and some large flares occur in association with emerging flux in developed active regions (Rust 1972; Zirin and Tanaka 1973; Canfield and Fisher 1976; Kundu and Woodgate 1986). These enhanced activities are considered to be due to the interaction between emerging flux and the preexisting magnetic field (Heyvaerts, Priest, and Rust 1977; Uchida and Sakurai 1977) or due to direct magnetic (current) energy transport by twisted emerging flux (Piddington 1975, 1976*a*, *b*; Parker 1974, 1979, p. 167; Tanaka 1987; Kurokawa 1988*b*; Uchida and Shibata 1988).

In contrast to the observational evidence of dynamical motion of emerging magnetic flux in the upper chromosphere or in the corona, there is not much evidence showing the dynamical emergence of magnetic flux in the photosphere. The rise velocities of emerging flux observed so far are very small (Chou and Wang 1987). Kawaguchi and Kitai (1976) reported rise velocities of the photospheric emerging loops as ≤ 0.2 km s^{-1}, and Brants (1985) found velocities $\simeq 1$ km s^{-1}. Kawaguchi and Kitai (1976) found also strong downdrafts with $\simeq 1.5$ km s^{-1} near sunspot pores, and Shibata (1980) interpreted them as the sliding flow due to gravity along rising magnetic loops similar to AFS.

Theoretically, the emergence of magnetic flux is believed to be due to magnetic buoyancy in the deep interior of the Sun (Parker 1955), which may be coupled with convective motion (Parker 1987, 1988). Many theoreticians have studied the

---

[1] Permanent address: Department of Earth Sciences, Aichi University of Education, Kariya, Aichi 448, Japan.

dynamical motion of magnetic flux in the convection zone of the Sun (e.g. Schüssler 1977, 1979, 1980; Meyer *et al.* 1979; Tsinganos 1980; Moreno-Insertis 1986; Choudhuri and Gilman 1987; Chou and Fisher 1989; Fisher, Chou, and McClymont 1988). Nonlinear two-dimensional magnetohydrodynamic (MHD) numerical simulations of emerging flux in the corona have been performed first by Nakagawa, Steinolfson, and Wu (1976) to see the dynamic response of the corona, and later by Forbes and Priest (1984) to see reconnection between emerging flux and overlying coronal magnetic field. However, no one has studied nonlinear two-dimensional MHD of magnetic flux emergence in the solar *photosphere* and *chromosphere*; i.e., in a gravitationally stratified gas layer with height greater than about $10H$, where H is the pressure scale height. Thus, our understanding of the physics of emerging magnetic flux in the solar photosphere and chromosphere is in a very preliminary stage.

In this paper, we will develop a two-dimensional MHD model of emerging magnetic flux in the solar photosphere/chromosphere and corona by using nonlinear two-dimensional MHD numerical simulations, and will try to clarify the physics of magnetic flux emergence by comparing numerical results with observational results discussed above. We study nonlinear evolution of the "Parker instability," the undular mode $[\boldsymbol{k} \parallel \boldsymbol{B}]$ of the magnetic buoyancy instability, where $\boldsymbol{k}$ and $\boldsymbol{B}$ are the wavenumber and magnetic field vectors (Parker 1966; Parker 1979, p. 314; Hughes and Cattaneo 1987), of a two-dimensional isolated magnetic flux sheet embedded in the bottom of the photosphere (or just below the photosphere). The rising magnetic loop resulting from the instability is identified as the emerging magnetic flux (Shibata *et al.* 1989). In our model, the rise velocity of the magnetic loop as well as the emerging rate of magnetic flux is determined self-consistently by the nonlinear dynamics of the Parker instability. This is in contrast to previous works on the numerical simulations of emerging flux in the corona by Nakagawa, Steinolfson, and Wu (1976) and Forbes and Priest (1984), both of which assumed ad hoc inflow with magnetic flux on the lower boundary of the computing domain, and did not explain how and why the magnetic flux emerges from below the photosphere. Although the main purpose of this paper is the application of simulation results to the dynamics of EFRs, we also study interaction and reconnection with overlying magnetic fields, such as network fields or preexisting active region fields.

Section II gives assumptions, basic equations, and numerical procedures. In § III, fundamental numerical results are shown, and in § IV we will compare numerical results with observational results. Finally, in § V, we present discussion and a summary.

II. METHODS OF NUMERICAL SIMULATIONS

a) *Assumptions and Basic Equations*

Assumptions, basic equations, and initial conditions are similar to those in Shibata *et al.* (1989) except for the new effect of magnetic diffusion. That is, we assume the following: (1) the medium is an ideal gas, (2) the gas is a polytrope of index $\gamma = 1.05$ for reasons discussed by Shibata *et al.* (1989), (3) the gravitational acceleration (g) is constant, (4) the evolution is two-dimensional (i.e., $\partial/\partial y = 0$, $B_y = 0$, $V_y = 0$). Cartesian coordinates (x, y, z) are adopted with orientation such that the z-direction is antiparallel to the gravitational acceleration vector. Thus, the basic equations in scalar form are as follows:

$$\frac{\partial \rho}{\partial t} + \frac{\partial}{\partial x}(\rho V_x) + \frac{\partial}{\partial z}(\rho V_z) = 0\,, \tag{1}$$

$$\frac{\partial}{\partial t}(\rho V_x) + \frac{\partial}{\partial x}\left[\rho V_x^2 + p + \frac{1}{8\pi}(B_z^2 - B_x^2)\right] + \frac{\partial}{\partial z}\left(\rho V_x V_z - \frac{1}{4\pi} B_x B_z\right) = 0\,, \tag{2}$$

$$\frac{\partial}{\partial t}(\rho V_z) + \frac{\partial}{\partial x}\left(\rho V_x V_z - \frac{1}{4\pi} B_x B_z\right) + \frac{\partial}{\partial z}\left[\rho V_z^2 + p + \frac{1}{8\pi}(B_x^2 - B_z^2)\right] + \rho g = 0\,, \tag{3}$$

$$\frac{\partial B_x}{\partial t} + \frac{\partial}{\partial z}\left(V_z B_x - V_x B_z - \frac{J_y}{R_m}\right) = 0\,, \tag{4}$$

$$\frac{\partial B_z}{\partial t} - \frac{\partial}{\partial x}\left(V_z B_x - V_x B_z - \frac{J_y}{R_m}\right) = 0\,, \tag{5}$$

$$\begin{aligned}
&\frac{\partial}{\partial t}\left[\frac{p}{\gamma - 1} + \frac{1}{2}\rho(V_x^2 + V_z^2) + \frac{1}{8\pi}(B_x^2 + B_z^2)\right] \\
&\quad + \frac{\partial}{\partial x}\left[\frac{\gamma}{\gamma - 1} p V_x + \frac{1}{2}\rho V_x (V_x^2 + V_z^2) + \frac{B_z}{4\pi}\left(V_x B_z - V_z B_x + \frac{J_y}{R_m}\right)\right] \\
&\quad + \frac{\partial}{\partial z}\left[\frac{\gamma}{\gamma - 1} p V_z + \frac{1}{2}\rho V_z (V_x^2 + V_z^2) + \frac{B_x}{4\pi}\left(V_z B_x - V_x B_z - \frac{J_y}{R_m}\right)\right] \\
&\quad + \rho g V_z = 0\,,
\end{aligned} \tag{6}$$

where J_y is the y-component of the normalized current density vector given by

$$J_y = \frac{\partial B_x}{\partial z} - \frac{\partial B_z}{\partial x} \tag{7}$$

and R_m is the magnetic Reynolds number defined by $C_s H/\eta$, where C_s and H are sound speed and pressure scale height in the initial magnetic flux region and η is the magnetic diffusivity. We take $R_m = 200$ for all models in this paper, in contrast to the assumption of $R_m = \infty$ in a previous paper (Shibata *et al.* 1989).

b) *Initial Conditions*

We consider a two-temperature gas layer as a very simplified model of the solar corona and chromosphere/photosphere. The distribution of the initial temperature is assumed to be

$$T(z) = T_{\rm ch} + (T_{\rm cor} - T_{\rm ch})\{\tanh\,[(z - z_{\rm cor})/w_{\rm tr}] + 1\}/2\,,$$

where $T_{\rm cor}/T_{\rm ch}$ is the ratio of the temperature in the corona to that in the chromosphere/photosphere, $z_{\rm cor}$ is the height of the base of the corona, $w_{\rm tr}$ is the temperature scale height in the transition region ($=0.6H$ for all our calculations, where H is the pressure scale height of the chromosphere/photosphere). We have calculated both the cases $T_{\rm cor}/T_{\rm ch} = 100$ and

$T_{\rm cor}/T_{\rm ch} = 25$ in some typical models and found that the results in the two cases are very similar. Thus we will show only the results with $T_{\rm cor}/T_{\rm ch} = 25$ in the following sections.

We assume that the magnetic field is initially parallel to the horizontal plane—$\boldsymbol{B} = (B_x(z), 0, 0)$—and is localized in the photosphere. The distribution of magnetic field strength is given by $B_x(z) = [8\pi p(z)/\beta(z)]^{1/2}$, where

$$\frac{1}{\beta(z)} = \frac{f_1(z)}{\beta_*} + \frac{f_2(z)}{\beta_{\rm cor}},$$

$$f_1(z) = \frac{1}{4}\left[\tanh\left(\frac{z - z_0}{w_0}\right) + 1\right]\left[-\tanh\left(\frac{z - z_1}{w_1}\right) + 1\right],$$

$$f_2(z) = \frac{1}{2}\left[\tanh\left(\frac{z - z_2}{w_2}\right) + 1\right].$$

Here β_* and $\beta_{\rm cor}$ are the ratios of gas pressure to magnetic pressure at the center of the magnetic flux sheet and in the corona, z_0 and $z_1 = z_0 + D$ are the heights of the lower and upper boundaries of the magnetic flux sheet, D is the vertical thickness of the magnetic flux sheet, and $z_2 = z_{\rm cor} + 1.5H$ is the base height of the coronal magnetic flux. Here the first term in the equation for $\beta(z)$ shows the magnetic flux in the photospheric flux sheet, and the second term shows the coronal field. The magnetic field strength is very small between the photospheric flux sheet and the coronal field (i.e., $z_1 < z < z_2$). It is assumed that $z_0 = 0$, $D = 4H$, $w_0 = w_1 = 0.5H$, $w_2 = 0.6H$, $\beta_* = 1$ for all our calculations. The origin of height z is taken to be at the bottom of the flux sheet, while the base of the computing box is taken to be $z = -4H$.

On the basis of the above initial plasma β distribution, the initial density and pressure distributions are numerically calculated by the equations of static pressure balance

$$\frac{d}{dz}\left[p + \frac{B_x^2(z)}{8\pi}\right] + \rho g = 0\,. \tag{8}$$

The initial gas pressure (p) and magnetic field strength (B_x) distributions for the case of $z_{\rm cor} = 14H$ and $\beta_{\rm cor} = \infty$ (model 1) are shown in Figure 1 with the initial temperature distribution.

The above magnetostatic gas layer is unstable for the Parker instability (Parker 1966). In order to start the instability, small velocity perturbations of the form

$$V_x = f_1(z) A C_s \sin\left[2\pi(x - x_{\rm max}/2)/\lambda\right]$$

are initially imposed on the magnetic flux sheet ($z_0 < z < z_1$) within the finite horizontal domain ($x_{\rm max}/2 - \lambda/2 < x < x_{\rm max}/2 + \lambda/2$), where λ ($= 20H$) is the horizontal wavelength of the small velocity perturbation, $x_{\rm max}$ ($= 80H$) is the horizontal size of the computing domain, and A ($= 0.05$) is the maximum value of V_x/C_s in the initial perturbation. This perturbation is not exactly the same as that for the unstable eigenfunction. However, the eigenfunction is numerically determined, and the growth rate of the perturbation in the linear regime agrees well with that obtained from the exact linear analysis (Shibata *et al.* 1989; see also Horiuchi *et al.* 1988; Matsumoto *et al.* 1988).

c) Boundary Conditions and Numerical Procedures

We assume periodic boundaries for $x = 0$ and $x = x_{\rm max}$, a symmetric (rigid conducting wall) boundary for $z = -4H$, and a free boundary for $z = z_{\rm max}$. The effect of the free boundary at $z = z_{\rm max}$ is small.

Equations (1)–(8) are nondimensionalized by using the following normalizing constants: H, C_s (the sound velocity in the chromosphere/photosphere), and ρ_0 (the density at the base of the gas layer, $z = -4H$). The units of length, time, and velocity are H, H/C_s ($= \tau$), C_s. The gas pressure, density, and magnetic field strength are normalized by $\rho_0 C_s^2$, ρ_0, and $(\rho_0 C_s^2)^{1/2}$, respectively. When we compare numerical results with observations, we will use $H = 200$ km, $C_s = 10$ km s^{-1}, $\tau = H/C_s = 20$ s, which are typical values for the solar chromosphere and photosphere. Equations (1)–(8) are then solved numerically by using a modified Lax-Wendroff scheme (Rubin and Burstein 1967) with artificial viscosity (Richtmyer and Morton 1967).

The mesh sizes are $\Delta z = 0.15$ or $\Delta z = 0.1$ for $z < z_{\rm cor}$ and slowly increasing for $z \geq z_{\rm cor}$, $\Delta x = x_{\rm max}/(N_x - 1)$, where N_x is the number of mesh points in the x-direction. The total number of mesh points is $(N_x \times N_z) = (101 \times 172)$, and the total area is $[x_{\rm max} \times (z_{\rm max} + 4H)] = (80H \times 34H)$ for model 1, $(80H \times 39H)$ for models 2 and 3, and $(80H \times 42H)$ for model 4.

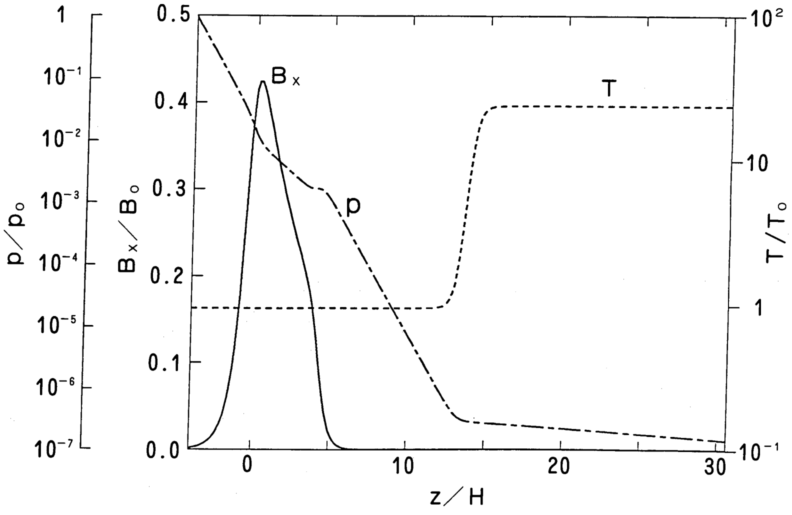

FIG. 1.—Initial distributions of gas pressure (p/p_0), magnetic field strength (B_x/B_0), and temperature (T/T_0), for model 1 ($\beta_* = 1$, $\beta_{\rm cor} = \infty$, $z_{\rm cor} = 14H$). Here $B_0 = (\rho_0 C_s^2)^{1/2}$, and ρ_0, p_0, T_0 are values at the base of the computing domain ($z/H = -4$). The unit of length is H, the scale height in chromosphere/photosphere.

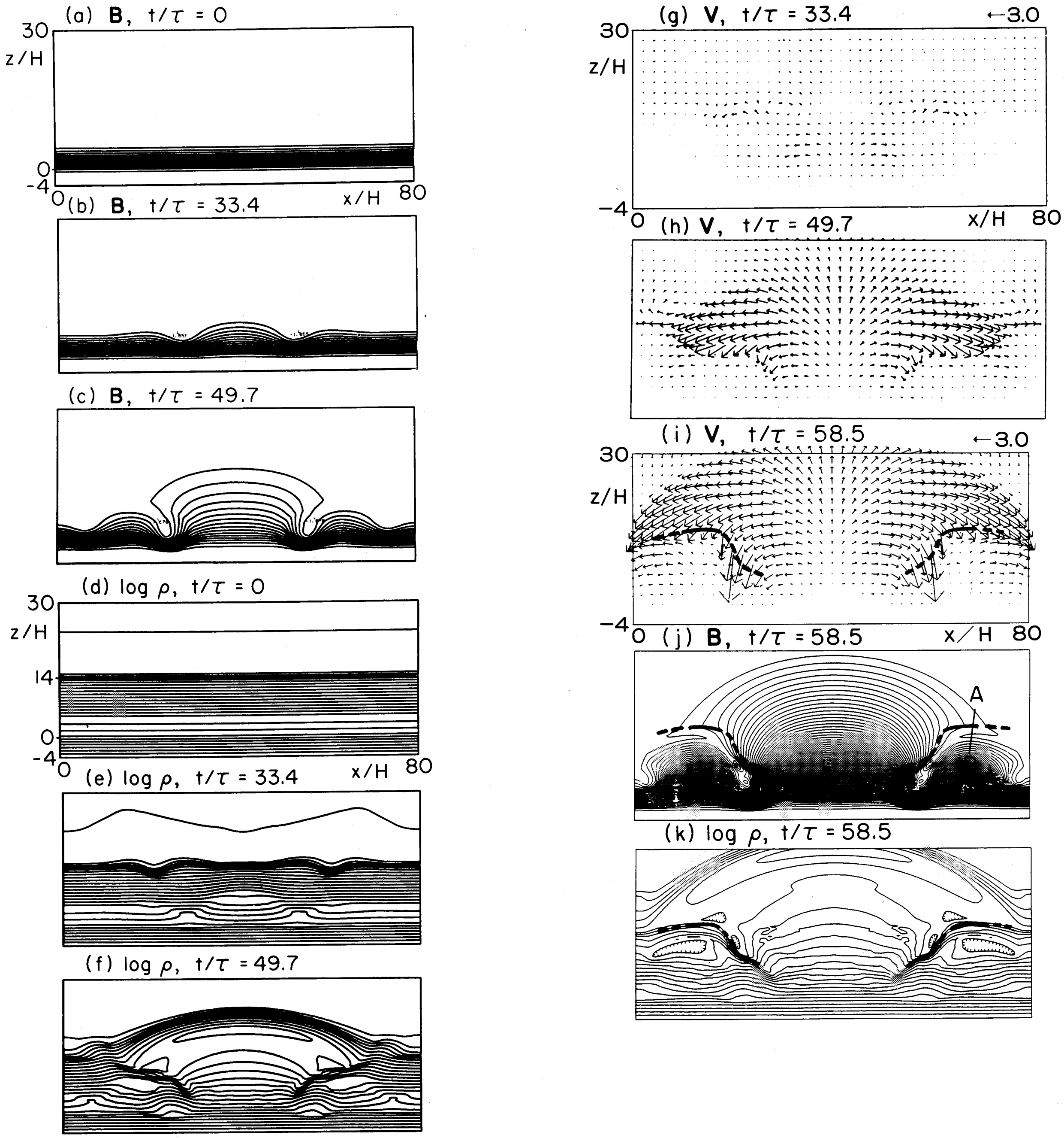

FIG. 2.—Results for model 1, where $\beta_* = 1$, $\beta_{\rm cor} = \infty$, $\lambda = 20H$, $z_{\rm cor} = 14H$. (*a*) Magnetic field lines $\boldsymbol{B} = (B_x, B_z)$ at $t/\tau = 0.0$, where $\tau = H/C_s$, (*b*) $\boldsymbol{B}$ at $t/\tau = 33.4$, (*c*) $\boldsymbol{B}$ at $t/\tau = 49.7$; (*d*) density contours $\log \rho$ at $t/\tau = 0.0$, (*e*) $\log \rho$ at $t/\tau = 33.4$, (*f*) $\log \rho$ at $t/\tau = 49.7$; (*g*) velocity vectors $\boldsymbol{V} = (V_x, V_z)$ at $t/\tau = 33.4$, (*h*) $\boldsymbol{V}$ at $t/\tau = 49.7$, (*i*) $\boldsymbol{V}$ at $t/\tau = 58.5$; (*j*) $\boldsymbol{B}$ at $t/\tau = 58.5$; (*k*) $\log \rho$ at $t/\tau = 58.5$. The contour level step widths are 0.3 for the density (ρ) in units of the logarithmic scale, and 0.1 in (*a*)–(*c*) and 0.02 in (*j*) for the magnetic flux in units of the linear scale. The scale of the velocity vector is shown above (*g*) and (*i*) in units of C_s.

III. NONLINEAR TWO-DIMENSIONAL DYNAMICS OF EMERGING MAGNETIC FLUX

a) Typical Nonlinear Evolution of Magnetic Flux Expansion Initiated by Parker Instability

If $\lambda \ll x_{\rm max}$, that is, if the wavelength of the magnetic loop is much smaller than the horizontal size of the computing domain, the nonlinear evolution of magnetic loop expansion, as a result of the Parker instability, is divided into three stages. The first stage is characterized by a self-similar evolution with exponential time dependence in a Lagrangian frame (or *nonlinear instability*). The second stage is also characterized by a self-similar expansion, but the time dependence becomes a power law. The final, third stage is a non–self-similar expansion stage, where the magnetic loop suffers strong deceleration to find a quasi-static equilibrium state at last. Figures 2 and 3 show results for model 1, which is a typical case suitable for emerging magnetic flux, and well illustrates the first and second

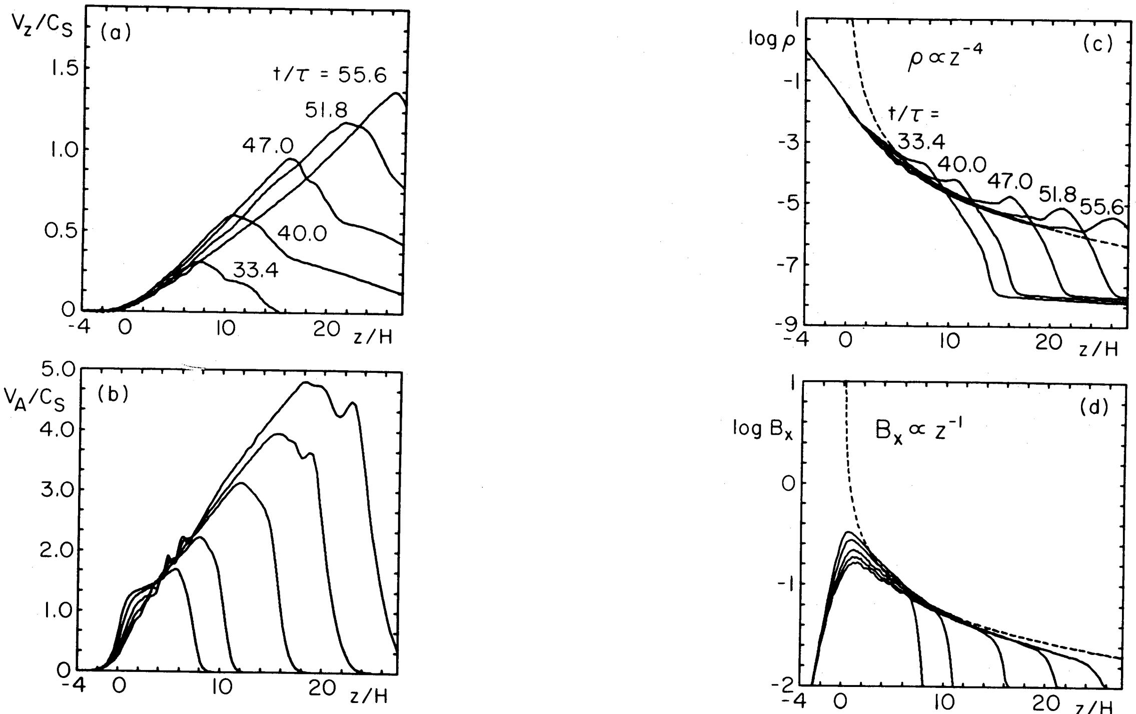

FIG. 3.—Distribution in z of (*a*) the vertical component of velocity (V_z), (*b*) the local Alfvén speed (V_A), (*c*) the density ($\log \rho$); (*d*) the horizontal component of the magnetic field ($\log B_x$), at $x = x_{\max}/2$ (middle of the rising loop) for model 1 (the case shown in Fig. 2) at $t/\tau = 33.4$, 40.0, 47.0, 51.8, and 55.6. The dashed curves in (*c*) and (*d*) indicate the curves of $\rho \propto z^{-4}$ and $B_x \propto z^{-1}$.

stages. In this model we assume $z_{\rm cor} = 14H$ and $\beta_{\rm cor} = \infty$, i.e., there is no magnetic field in the corona. In the following, we will discuss each stage in more detail, and examine the dynamical structure and energetics of expanding magnetic flux. It should be noted that the results shown in Figures 1 and 2 are very similar to those in a previous paper (Shibata *et al.* 1989), although $R_m = 200$ is assumed in Figures 1 and 2, while $R_m = \infty$ was assumed in Shibata *et al.* (1989).

i) *First Stage* ($30 < t/\tau < 50$): *Exponential Expansion*

When the top of the magnetic loop is below the base altitude of the corona, the rise velocity of the magnetic loop increases linearly with height (Fig. 3*a*). The velocity is nearly constant in an Eulerian frame, while in a Lagrangian frame it increases exponentially with time. This expansion law is written (Shibata *et al.* 1989) as

$$V_z/C_s = a_1 z/H = a_1 \xi \exp (a_1 t) , \tag{9}$$

where z is the height measured from the base of the initial magnetic flux sheet, $a_1 = 0.05$–0.07 for $\beta_* = 0.5$–2.0 is about half the linear growth rate, ξ is the Lagrangian coordinate, and H and C_s are the pressure scale height and sound speed in the low-temperature atmosphere (photosphere and/or chromosphere). The mass density (Fig. 3*c*), the horizontal component of the magnetic field (Fig. 3*d*), and the local Alfvén speed (Fig. 3*b*) at the midpoint of the loop are

$$\rho \propto \xi^{-4} \exp (-4a_1 t) \propto z^{-4} , \tag{10}$$

$$B_x \propto \xi^{-1} \exp (-a_1 t) \propto z^{-1} , \tag{11}$$

$$V_A/C_s = a_2 \xi \exp (a_1 t) = a_2 z/H , \tag{12}$$

where $a_2 \simeq 0.2$–0.4 for $\beta_* = 0.5$–2.0. Since $V_A/C_s \gg 1$ (or $\beta \ll 1$) in the higher layer, the magnetic field tends to be current-free (thus force-free) as the magnetic loop expands to higher layers.

ii) *Second Stage* ($50 < t/\tau < 55 - 60$): *Power-Law Expansion*

After the loop enters the corona, the expansion law changes from an exponential-law to a power-law increase given by

$$V_z = \alpha z/t = \alpha t^{\alpha - 1} \xi , \tag{13}$$

$$\rho \propto z^{-4} , \tag{14}$$

$$B_x \propto z^{-1} , \tag{15}$$

where $\alpha \simeq 5$ for $\beta_* \simeq 1$. That is, the steady distributions of the density and magnetic field strength are the same as in the first stage, while the velocity evolution is different from that of the first stage; the rise velocity of the magnetic loop decreases with time in an Eulerian frame, but it still increases in a Lagrangian frame.

Shibata *et al.* (1989) have shown that the nonlinear expansion of a magnetic loop in the first and second stages is due to magnetic pressure force, although the dynamics are controlled by the downflow due to gravity along the rising loop; the evacuation by the downflow increases the local Alfvén speed of the loop, leading to acceleration of the magnetic loop. Consequently, as long as the magnetic pressure at the top of the magnetic loop is larger than the coronal total (gas and magnetic) pressure, the expansion of the magnetic loop continues.

iii) *Final Stage* ($60 < t/\tau$): *Quasi-static Equilibrium State*

After the loop reaches the height z_d where the magnetic pressure at the top of the expanding magnetic loop becomes comparable to the coronal total (gas and magnetic) pressure, the loop suffers strong deceleration by coronal pressure. We estimate the critical height z_d in the following. The approximate initial gas pressure p_g is given by $p_g = p_{g,0} \exp(-z/H)$ for the chromosphere ($z \leq z_{\rm cor}$), and $p_g = p_{g,\rm cor} \simeq p_{g,0} \exp(-z_{\rm cor}/H)$ for corona ($z > z_{\rm cor}$), where $p_{g,0}$ is the gas pressure at $z = 0$. Here we assumed that the coronal gas pressure is constant because the scale height is very large in the corona because of the high temperature. Thus, the total coronal pressure is $P_{\rm cor} = p_{g,\rm cor} + p_{m,\rm cor} = p_{g,\rm cor}(1 + 1/\beta_{\rm cor})$, if we assume $\beta_{\rm cor} =$ constant in the corona. On the other hand, the magnetic pressure at the top of the loop (p_m) scales as $p_m = p_{m,H}(z/H)^{-2}$ by using equation (11), where $p_{m,H}$ is the magnetic pressure at $z = H$. We assume $p_{m,H} = p_g\,(z = H) = p_{g,0}/e$ as in model 1 ($\beta_* = 1$). Then the height z_d where $P_{\rm cor} = p_m$ is

$$z_d/H = (1 + 1/\beta_{\rm cor})^{-1/2}(p_{g,\rm cor}/p_{g,0})^{-1/2}e^{-1/2}$$
$$= (1 + 1/\beta_{\rm cor})^{-1/2} \exp\,[z_{\rm cor}/(2H)]e^{-1/2}\,. \qquad (16)$$

Thus, for model 1 ($\beta_{\rm cor} = \infty$, $z_{\rm cor}/H \simeq 14$, $p_{g,\rm cor}/p_{g,0} \simeq 10^{-6}$), we obtain $z_d/H \simeq 600$. In this case the strong deceleration does not take place in the computing domain ($z \leq 31H$). For models 2 and 3 in § IIIb ($\beta_{\rm cor} = 0.5$, $z_{\rm cor}/H \simeq 11$, $p_{g,\rm cor}/p_{g,0} \simeq 2 \times 10^{-5}$), we have $z_d/H \simeq 80$.

In the above we neglected the magnetic tension force. Actually, however, this force cannot be neglected and exerts an additional decelerating force. Thus, when there is a strong magnetic field ($\beta_{\rm cor} < 1$), the magnetic loop ceases to expand at a height smaller than z_d.

iv) *Shocks and Neutral Sheets in the First and Second Stages*

Figure 2 shows the existence of strong MHD shock waves near the footpoints of the loop. Shocks occur, since the maximum downflow speed is about $4C_s$–$5C_s$, which exceeds the local sound speed and the Alfvén speed ($V_{\rm A} \simeq 2C_s$–$4C_s$). The structure of the shock is not simple, but we can identify a fast MHD shock in the lower region and an intermediate MHD shock in the upper region (just above the neighboring loop). The approximate location of the shocks is indicated on panels *i*, *j*, and *k* of Figure 2, with dashed lines representing the fast shock and the longer solid lines the intermediate shock.

Fast-mode MHD shocks occur when the upstream velocity relative to the shock front exceeds the fastest characteristic speed. These shocks have been studied extensively (e.g., Kantrowitz and Petschek 1966) and will not be described further here. It has only recently been recognized that MHD intermediate shocks may be found in multidimensional situations (Steinolfson and Hundhausen 1988), and therefore we will discuss some of the features of such shocks. Intermediate shocks differ from fast and slow shocks in that, unlike these shocks, there is not an analogous compressive intermediate wave that may steepen to form the shock. However, as demonstrated by Steinolfson and Hundhausen, they may form in environments where adjacent (crossflow) regions have the opportunity to interact with and influence each other. A primary difference between intermediate shocks and the other two types is that the component of the magnetic field parallel to the shock plane reverses direction across an intermediate shock, while it retains its direction across the others. Whereas the magnetic field strength increases across fast shocks and decreases across slow shocks, it may either increase or decrease across an intermediate shock. Steinolfson and Hundhausen also showed how fast and intermediate shocks can merge continuously along a shock front.

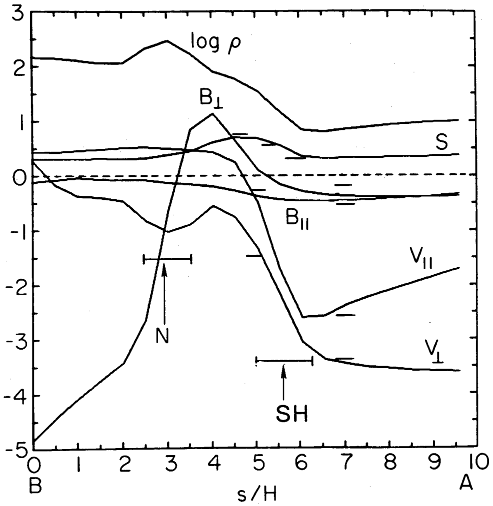

FIG. 4.—Distributions of some physical quantities along the short line *A*–*B* shown in Fig. 2; density (log ρ), entropy (S), magnetic field strength perpendicular to the shock normal ($100 \times B_\perp$), magnetic field strength parallel to the shock normal ($100 \times B_\parallel$), velocity perpendicular to the shock normal ($V_\perp$), velocity parallel to the shock normal ($V_\parallel$). The arrows labeled N and SH indicate the positions of the neutral sheet and the (intermediate) shock. The values shown by the short horizontal lines upstream of the shock (*right-hand side*) were used in the MHD shock jump equation to compute the downstream values, which are also indicated by short horizontal lines (*left-hand side*).

The fact that an intermediate shock is formed can be seen by the variation of the physical quantities through the shock as shown in Figure 4. The line along which these changes occur is the span *A*–*B* indicated on Figure 2*j*. This span is selected to be approximately perpendicular to the shock front. The values shown by the short horizontal lines upstream of the shock were used in the MHD shock jump equation to compute the downstream values, which are also indicated by short horizontal lines. The shock velocity was determined by comparing the shock locations at successive times. Although the agreement with the shock jump equations is not exact, the changes computed from the shock jump equations are consistently smaller than those in the numerical simulation in a systematic fashion. In addition, the numerical solution does show the reversal of the perpendicular magnetic field, $B_\perp$, characteristic of an intermediate shock. There are several reasons why one may not expect exact agreement with planar shock jump conditions. For instance, upstream and downstream conditions are not uniform in space and are rapidly changing with time. It is also difficult to identify appropriate upstream conditions and shock velocity for the shock calculation.

Magnetic reconnection may occur in the neutral sheet created just below the downflow. However, the evidence of slow MHD shocks typical of fast reconnection (Petschek 1964; Ugai and Tsuda 1977; Tsuda and Ugai 1977; Sato and Hayashi 1979) is not found in this case, similar to the results of Brunel, Tajima, and Dawson (1982).

v) *Energetics*

Figure 5 shows the time variation of magnetic, gravitational, and kinetic energy in the system. The magnetic (E_m) and gravitational (ΔE_g) energies decrease with time, while the kinetic energy (E_k) slightly increases with time, although it is much smaller than the magnetic and gravitational energies. Most of the released energy is converted into thermal energy through compressional and shock heating; $E_m + \Delta E_g + E_k \simeq -\Delta E_{\rm th}$. (It should be noted that $\Delta E = E(t) - E(0)$ for ΔE_g and $\Delta E_{\rm th}$.)

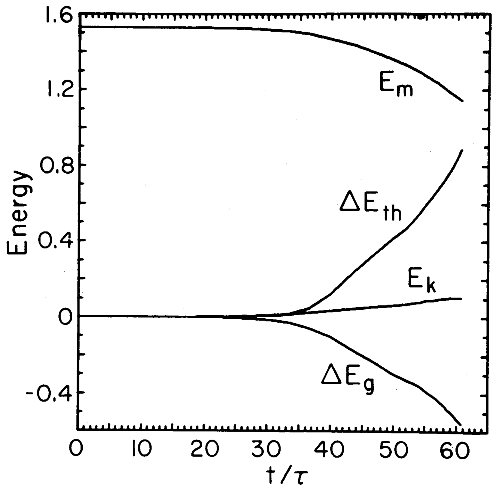

FIG. 5.—Time variations of magnetic (E_m), thermal (ΔE_{th}), kinetic (E_k), and gravitational (ΔE_g) energies contained in a computing domain, where $\Delta E = E(t) - E(0)$.

This is the same as in the Parker instability of galactic (or accretion) disks with continuous magnetic field distribution studied by Matsumoto *et al.* (1988). However, in the latter case the decrease in magnetic energy is much smaller than that in the gravitational energy, while in our case the magnetic energy significantly decreases, and the total released magnetic energy is comparable to that of the gravitational energy. This is because there is no overlying magnetic field in our problem so the magnetic field can freely expand upward to reduce its energy as long as the loop is in the chromosphere. The influence of the overlying field is addressed in the next section. The rate of decrease in magnetic energy is given by

$$\frac{dE_m}{dt} \simeq -\frac{10^{-2}E_m}{(H/C_s)},$$

$$= -5 \times 10^{27} \text{ ergs s}^{-1}\left(\frac{E_m}{10^{31}\text{ ergs}}\right)\left(\frac{H}{200\text{ km}}\right)^{-1} \times \left(\frac{C_s}{10\text{ km s}^{-1}}\right), \qquad (17)$$

where E_m is the magnetic energy stored in the initial horizontal magnetic flux sheet just below the photosphere, and is equal to 10^{31} ergs when the length, width, and height of the flux are $80H$, $40H$, and $4H$, respectively, and $H = 200$ km. Most of the initial magnetic energy is released in a time of about

$$100H/C_s = 30 \text{ minutes } (H/200\text{ km})(C_s/10\text{ km s}^{-1})^{-1}.$$

b) Interaction with Overlying Magnetic Fields

i) *Parallel Case (Model 2)*

We now study the effect of overlying horizontal coronal magnetic fields on the expansion of an emerging magnetic loop, and the results are shown in Figure 6. In this case, it is assumed that $z_{\rm cor} = 11H$ and $\beta_{\rm cor} = 0.5$. The coronal field decelerates the expansion of the magnetic loop after $t/\tau \simeq 50$, and the velocity distribution in height deviates from a linear distribution (see Fig. 7). The coronal magnetic fields interact with the emerging field, forming a continuous distribution of approximately current-free field with $B_x \propto z^{-1}$.

ii) *Antiparallel Case (Model 3)*

Figure 8 shows the case with antiparallel coronal field. Other parameters are the same as in the case of Figures 6 and 7. This case involves physics similar to the coalescence model of flares (Tajima *et al.* 1987). We see that a neutral (current) sheet is created between the emerging flux and the coronal field, and the density (and thus the pressure) is enhanced within the sheet as seen in Figure 8*c*. The most remarkable result in this case is that the expansion of the magnetic loop is *not* decelerated even after the loop is in contact with the coronal field. On the other hand, the magnetic flux above the neutral

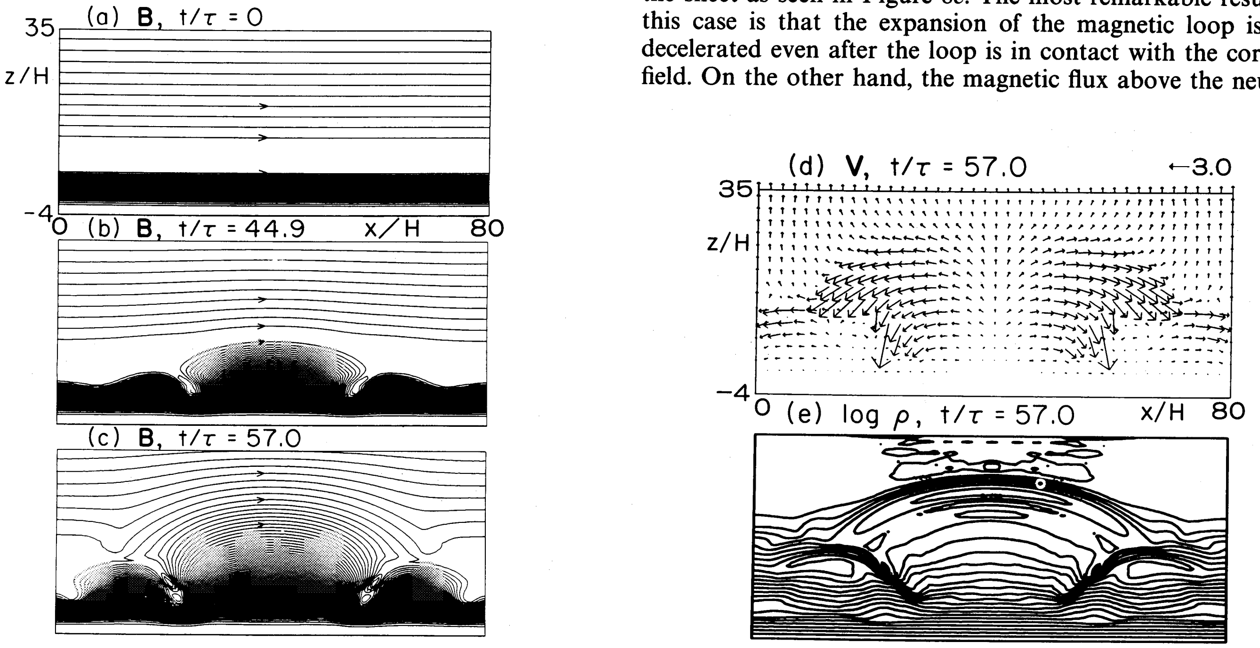

FIG. 6.—Results for model 2, where $z_{\rm cor} = 11H$, $\beta_{\rm cor} = 0.5$, and the coronal field is parallel to the emerging flux. (*a*) Magnetic field lines ***B*** at $t/\tau = 0.0$, (*b*) ***B*** at $t/\tau = 44.9$, (*c*) ***B*** at $t/\tau = 57.0$, (*d*) velocity vectors (***V***) at $t/\tau = 57.0$, (*e*) density contours ($\log \rho$) at $t/\tau = 57.0$. Other remarks are the same as in model 1 (Fig. 2).

1989ApJ...345..584S

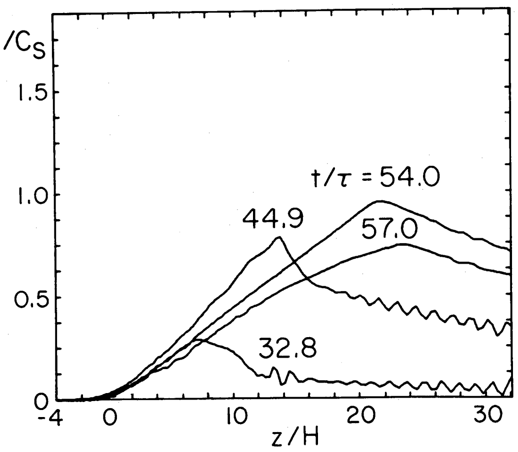

FIG. 7.—Distribution in z of the vertical component of velocity, V_z, in model 2 (the case shown in Fig. 6) at t/τ = 32.8, 44.9, 54.0, and 57.0.

sheet is not strongly accelerated upward even after emerging flux collides with the neutral sheet. The vertical velocity at the midpoint of the loop increases linearly with height up to the neutral sheet, and then steeply decreases in the neutral sheet (see Fig. 9*a*). Thus, there is a sink of mass and magnetic flux in the neutral sheet due to magnetic reconnection, and the accumulated mass and magnetic flux are convected in the horizontal direction along the neutral sheet.[2]

Furthermore, a jet flow ($V_x \simeq 2C_s \simeq 0.3V_A$ at $x = 48H$) is produced along, but just below, the neutral sheet in later stage (see Fig. 9*b*), which is difficult to distinguish from the downflow due to gravity in a two-dimensional figure, but is easily recognized in a one-dimensional distribution of V_x at $x = x_{\max}/2 + 8H = 48H$. This jet-type flow is produced by magnetic

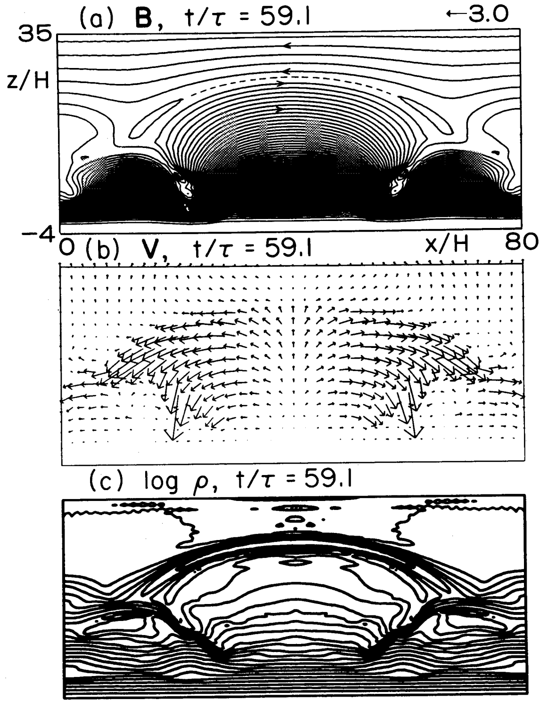

FIG. 8.—Results for model 3, where $z_{\rm cor} = 11H$, $\beta_{\rm cor} = 0.5$, and the coronal field is antiparallel to the emerging flux. (*a*) Magnetic field lines (***B***), (*b*) velocity vectors (***V***), (*c*) density contours (log ρ). All these are at t/τ = 59.1. The position of the neutral sheet is indicated by the dashed curve. Other remarks are the same as in model 1 (Fig. 2).

reconnection similar to the dayside magnetospheric reconnection (Hoshino and Nishida 1983; see also Leboeuf *et al.* 1978). The gas pressure in the corona is much larger than that in the magnetic loop, and the jet-type flow is accelerated along the field line by the gas pressure gradient which is created by magnetic reconnection between the high gas pressure (coronal) tube and the low gas pressure (emerging flux) tube. A similar

---

[2] The half-thickness of the current sheet in simulation results is about $2H$, which includes 10 grid points. Thus, the reconnection region is well resolved. This value is larger than the theoretical value ($\sim 0.2H$) for $R_m = 200$ according to the Sweet-Parker theory (e.g., Priest 1982, p. 348). Although the Sweet-Parker theory cannot be directly applied to our results because the reconnection is nonsteady and compressible in our simulations, this suggests that the effective magnetic Reynolds number in the current-sheet region may be smaller than the assumed value 200.

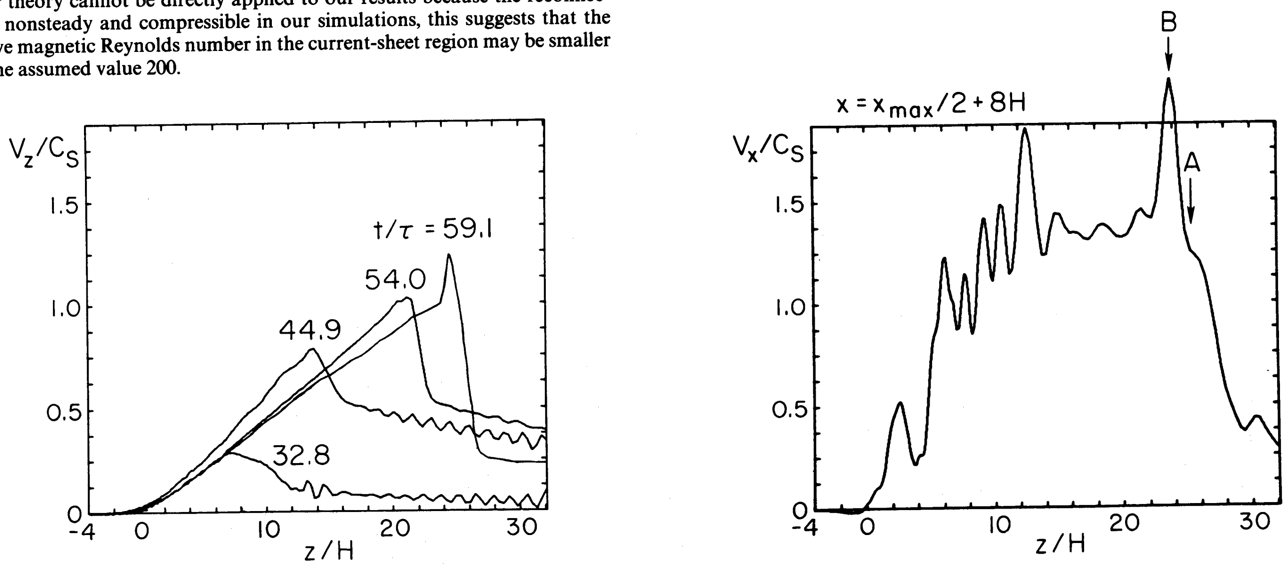

FIG. 9*a* FIG. 9*b*

FIG. 9.—Distribution in z of (*a*) the vertical velocity V_z at the midpoint of the loop (at $x = x_{\max} = 40H$) for t/τ = 32.8, 44.9, 54.0, and 59.1, and (*b*) the horizontal component of velocity V_x at $x = x_{\max} + 8H = 48H$ for t/τ = 59.1, in model 3 (the case shown in Fig. 8). The arrows labeled A and B in (*b*) show the positions of the neutral sheet and the jet-type flow, respectively.

flow driven by gas pressure drop along the field line developed during the reconnection is also studied by Brunel, Tajima, and Dawson (1982). A different mechanism for the generation of a jet flow associated with the reconnection is discussed by Soward and Priest (1986).

IV. COMPARISON WITH OBSERVATIONAL FACTS

In this section we compare numerical results with some observations. Considering the many uncertainties in the observational data and the idealized situation in the numerical simulations, we caution that our comments in this section should not be taken too literally. However, we believe that such comparisons are instructive or helpful for future research. In the present case, the comparisons are at least suggestive of a mechanism similar to the Parker instability considered above.

*a) Summary of Observations on EFR*s

Here we will summarize key observational data that assist in understanding the nonlinear dynamics in EFRs (see Fig. 10). The first appearance of emerging flux in the solar photosphere may be a tiny bipolar magnetic element observed in magnetograms, or perhaps a *granular dark lane* observed in the white light granules in the photosphere (Bray and Loughhead 1964, p. 64; Brants and Steenbeck 1985; Zwaan 1985). Faculae or pores are observed near the edges of dark lanes. The next observational evidence for emerging flux in the photosphere is *strong downdrafts* near pores (Kawaguchi and Kitai 1976; Bumba 1967; Brants 1985). The downflow speed parallel to the line-of-sight direction is 1–2 km s^{-1} at the photospheric level. Since the tube is nearly horizontal between two polarities, the actual downflow speed along the loop may be much larger (Shibata 1980). The rise velocity is very small in the photosphere, and observation gives a velocity of less than 1 km s^{-1} (Kawaguchi and Kitai 1976; Brants 1985; Chou and Wang 1987; Tarbel *et al.* 1988). However, this may be due to low spatial resolution, and the actual rise velocity may be even larger.

The first chromospheric response to emerging flux is Hα (*or* Ca II) *brightening* or *bright plages* (Bumba and Howard 1965; Born 1974; Glackin 1975; Kawaguchi and Kitai 1976). On the other hand, Kurokawa (1988*a*) found that the first manifestation of emerging flux in Hα is a surge activity (see also Marsh 1978). The first arch of an AFS appears in Hα from 1 hr (Glackin 1975) to about 1.5 hr (Kawaguchi and Kitai 1976) following the initial Hα brightening. The rise velocity of filaments is 10–15 km s^{-1} (Bruzek 1967, 1969; Chou and Zirin 1988; Suematsu 1987), and the downflow along the filament amounts to 30–50 km s^{-1}. Unfortunately, there is no observational information on the rise velocity of the magnetic loop between arch filaments and photospheric emerging magnetic flux. The length of filaments (as well as the size of an AFS) is (1–3) × 10^4 km. The lifetime of individual filaments is about 20 minutes (Bruzek 1967). At this stage, *moving magnetic features* (MMFs) with a horizontal velocity of 0.5–2 km s^{-1} are frequently observed at the foot of the arch filaments in magnetograms.

b) Dynamics of Individual Filaments in AFSs

The rise velocity of the magnetic loop obtained from our numerical simulations is analytically given in equation (9) for the first stage, which is shown again here by using typical numerical constants for emerging flux:

$$V_z \simeq 12 \text{ km s}^{-1}\left(\frac{z}{4000 \text{ km}}\right)\left(\frac{H}{200 \text{ km}}\right)^{-1}\left(\frac{C_s}{10 \text{ km s}^{-1}}\right). \tag{18}$$

This equation is applied up to about $z \simeq 20H \simeq 4000$ km if $H = 200$ km, beyond which the expansion law changes to that given by equation (13) for the second stage. According to the numerical simulations, the second stage is somewhat short, and the rise velocity does not increase as much. The maximum speed is about $V_z \simeq 1.5C_s \simeq 15$ km s^{-1} for model 1, if $C_s = 10$ km s^{-1}. In the third stage, the maximum velocity of the loop gradually decreases with height up to $z_a \simeq 60{,}000$ km for model 1. Therefore, the rise velocity of the magnetic loop pre-

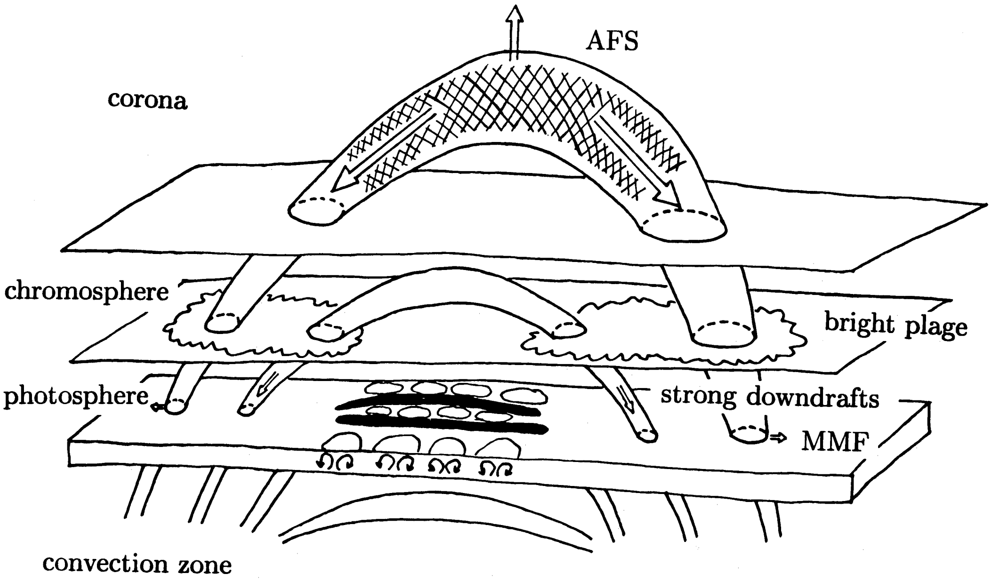

FIG. 10.—Schematic picture of emerging flux regions

dicted by numerical simulations is about 10–15 km s^{-1} for $3000 < z < 10{,}000$ km. This value agrees very well with the observed rise velocity of the individual arch filaments (Bruzek 1969; Chou and Zirin 1988; Suematsu 1987). The downflow speed found in simulations is about $3C_s$–$5C_s = 30$–50 km s^{-1} in the upper chromosphere ($10 < z/H$, or 2000 km $< z$). This value is also consistent with observed downflow speeds (Bruzek 1969).

Let us now consider the length of the filament. Numerical simulations (Fig. 1) show that the length of the loop increases with height as

$$l \simeq 2z + l_0 \,, \tag{19}$$

for $z \leq 30H = 6000$ km, where l_0 is the initial wavelength ($\simeq 20H$, the most unstable wavelength of Parker instability for the photospheric magnetic flux with $\beta \simeq 1$). Thus, $l \simeq 40H$–$80H \simeq 8000$–$16{,}000$ km, when the loop reaches the height $z \simeq 10H$–$30H \simeq 2000$–6000 km. For $z \geq 30H$, the loop length may be even larger than that given by equation (19). These results are consistent with the observed length of the filaments.

c) *Bright Plages and Enhanced Activities*

Simulations show that strong shock waves are formed near the footpoints of the magnetic loop. These shock waves may be related to bright plages observed near the foot of the AFSs. We will estimate the energy loss rate by the shock just below the downflow. According to our numerical results, the downflow speed, $v_{\rm df}$, is of order $3C_s$–$5C_s \simeq 30$–50 km s^{-1}. The particle number density in the magnetic loop (filament) is about 10^{11} cm^{-3} (Chou and Zirin 1988), or the mass density (ρ) is about 10^{-13} g cm^{-3}. Then the kinetic energy flux through the shock front, which is assumed here to be radiated away, is $F \sim \frac{1}{2}\rho v_{\rm df}^2 \times v_{\rm df} \sim 6 \times 10^6$ ergs s^{-1} cm^{-2}. Since the area of the footpoint of the loop is of the order of $A \sim 10^{18}$ cm, the total energy loss rate is $L \sim FA \sim 6 \times 10^{24}$ ergs s^{-1}. These are comparable to the observed values (e.g., Svestka 1976, p. 13). Thus, the kinetic energy of downflow, whose ultimate origin is the magnetic energy stored in the initial magnetic flux sheet (discussed below), explains a part of the chromospheric heating in EFRs.

The release rate of magnetic energy stored in the initial photospheric magnetic flux given in equation (17) is about 5×10^{27} ergs s^{-1}, if the length, width, and height of the initial magnetic sheet are 16,000 km ($= 80H$), 8000 km ($= 40H$), and 800 km ($= 4H$). This corresponds to an energy flux of about 4×10^9 ergs cm^{-2} s^{-1}, which is much larger than the energy flux required for the heating of active region chromosphere and corona (Priest 1982, p. 206). According to numerical results in Figure 5, almost all released magnetic energy is converted to thermal (internal) energy of the plasma through compressional and shock heating. It should be noted that this energy release is simply due to the expansion of magnetic flux; no exotic mechanism such as anomalous current dissipation is necessary. Consequently, from the energetics point of view, the enhanced activites in EFRs are easily understood as due to the release of magnetic energy stored in the magnetic flux in or below the photosphere when the magnetic flux expands upward into the chromosphere and the corona.

d) *Emerging Flux in the Photosphere and Strong Downdrafts near Pores*

Equation (18) shows that the rise velocity of emerging flux in the photosphere ($z \leq 500$ km) is less than 1.4 km s^{-1}. This value is consistent with observed small rise velocities of emerging flux in the photosphere (Kawaguchi and Kitai 1976; Brants 1985; Tarbel *et al.* 1988). Our simulations also shows transient strong downdrafts at the footpoint of the magnetic loop ($z \simeq 2.5H \simeq 500$ km) in the early stage of the magnetic loop expansion: the vertical component of the flow is $V_z \simeq 1$–3 km s^{-1}, and the horizontal component is $V_x \simeq 3$–6 km s^{-1} with a duration of about 200 s. After this transient strong downdraft stage, the flow undergoes damping oscillations whose period is approximately the sound travel time along the loop. These features agree fairly well with those in a one-dimensional simulation model of Shibata (1980), and thus explain strong downdrafts observed by Kawaguchi and Kitai (1976).

e) *Other Points*

i) *Time Scale of EFR Evolution*

According to our numerical results, the time scale for the emergence of magnetic flux from the bottom of the atmosphere to the coronal level ($z \simeq 10H \simeq 2000$ km) is about $50H/C_s$–$60H/C_s \simeq 1000$–1200 s, or about 20 minutes. This is comparable to the observed time difference ($\simeq 30$ minutes) between the first appearance in magnetograms and Hα brightenings (or the appearance of bright plage) (Harvey and Martin 1973). It takes about another 20–30 minutes or more for the magnetic loop to reach the level $z \simeq 50H$–$100H \simeq 10{,}000$–$20{,}000$ km in our results. This time is comparable to the observed time difference between the first Hα brightening (or strong downdraft in the photosphere) and the first appearance as AFSs (Glackin 1975; Kawaguchi and Kitai 1976).

ii) *Reconnection and Surges*

In § III*b* we have seen that the rise velocity of a magnetic loop is significantly suppressed when the field direction in the loop is parallel to that of the overlying coronal field, while it is *not* decelerated when both fields are antiparallel because magnetic reconnection occurs between them. We can use this result as a diagnostic for the pattern of the interaction between the emerging flux and an overlying preexisting field. That is, if the preexisting field is not very weak, and yet the observed rise velocity of the emerging filament is of the order of 10 km s^{-1} in Hα, we can say that magnetic reconnection is occurring. On the other hand, if we observe a much smaller rise velocity for the emerging flux, the magnetic reconnection is not occurring. Actually, the angles between the emerging flux and the preexisting fields are between 180° and −180°, and so the rise velocities of filaments may have intermediate values. It may be interesting to study observationally the correlation of rise velocities of emerging (AFS) filaments with angles between filaments and overlying fields.

We also observed in model 3 that a jet-type flow occurs along the reconnected field line. Although the velocity of the flow is not large ($\sim 2C_s$–$4C_s \simeq 20$–40 km s^{-1}), this flow may explain some small surges observed in EFRs (Marsh 1978; Kurokawa 1988*a*).

iii) *Ephemeral Region with No Signature of a Coronal EFR*

The fact that there are many ephemeral regions with no coronal signature of an EFR is usually attributed to their small magnetic flux (e.g., Harvey and Martin 1973; Chou and Wang 1987). Here we propose another possibility: The expansion of magnetic flux is stopped by the large coronal (magnetic and/or gas) pressure (as explained in § III). Figure 11 shows such an example (model 4; $z_{\rm cor} = 9H$, $\beta_{\rm cor} = 0.5$), where the magnetic loop is completely stopped below the corona, so that there is

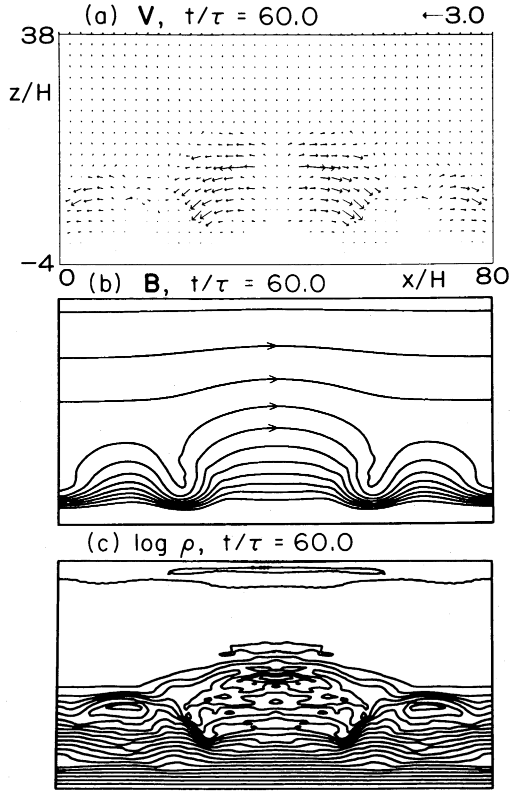

FIG. 11.—Results for model 4, where $z_{\rm cor} = 9H$, $\beta_{\rm cor} = 0.5$, and the coronal field is parallel to the emerging flux. (*a*) Velocity vectors (***V***), (*b*) magnetic field lines (***B***), (*c*) density contours (log ρ), all at $t/\tau = 60.0$. Other remarks are the same as in model 1 (Fig. 2).

no strong downflow along the loop. The maximum values of the rise velocity of the loop and the downflow at $t/\tau = 60$ are $0.3C_s = 3$ km s^{-1} and $2.3C_s = 23$ km s^{-1}, respectively.

If we apply the above argument to the emergence of magnetic flux tubes in the region with low coronal pressure (e.g., coronal holes, according to Shibata and Suematsu 1982), we predict that the rise velocities and the downflows in AFS filaments are larger in coronal holes than those in (normal) quiet regions by 10%–20%.

iv) *Magnetic Flux Distribution below the Photosphere*

Our simulation results show that if there is a horizontal flux sheet (or tube) in the bottom of the photosphere (or just below the photosphere), multiple loops are formed whose wavelengths are about $20H \simeq 4000$ km and whose footpoints are on a single line, for example, p–m–$p \cdots$–m–p–m, where p and m denote the plus and minus polarities and the dashes denote the loops. However, observations indicate that there is usually one loop (or one aggregation of loops) between two opposite polarities except for the case of flux emergence in complex active regions. This means that the horizontal part of the flux tube just below the photosphere is at most of the order of 10^4 km. If the flux tube rises directly from the bottom of the convection zone, the wavelength is of the order of $10H_{\rm cb}$–$20H_{\rm cb}$, where $H_{\rm cb}$ is the pressure scale height at the bottom of the convection zone and is about 10^4–10^5 km. Then the wavelength of the rising tube is about 10^5–10^6 km, so that the top of the tube may be nearly horizontal. In this case, multiple loops on one line like those mentioned above will occur. But, this is not the case in the actual Sun. Consequently, we hypothesize that the magnetic flux tube has smaller structure just below the photosphere than at the bottom of the convection zone, and the typical length (or the curvature radius) of the tube is determined by the size of the turbulence, which may be the size of supergranulation ($\simeq 10^4$ km). Figure 12 illustrates our picture. This picture may be relevant to the ephemeral active regions (Golub *et al.* 1981; Parker 1988).

V. SUMMARY AND DISCUSSION

1. The nonlinear expansion of emerging magnetic flux initiated with the Parker instability (undular mode of magnetic buoyancy instability) is divided into three stages. The first stage is when the top of the loop is below the base height of the corona, and is characterized by the approximate self-similar expansion with exponential time dependence in a Lagrangian frame. The second stage starts after the loop enters the corona and continues until it begins to suffer strong deceleration by coronal pressure. During this stage, the loop evolution is approximately self-similar, although the time dependence is a power law. The third (final) stage is after the loop begins to be decelerated, and the loop expands non–self-similarly, being decelerated to find a quasi-static equilibrium state.

2. In the first and second stages the rise velocity of the loop and the local Alfvén speed in the loop increase with height up to about 4000 km, and the duration of the first and second stages is about $30H/C_s$–$60H/C_s \simeq$ 10–20 minutes. The rise velocity of the loop and the downflow along the loop at $z \simeq 4000$ km are 10–15 km s^{-1} and 30–50 km s^{-1}, respectively, and are consistent with observed velocities in AFSs.

3. The rise velocity of the loop in the photosphere ($z \leq 500$ km) is ≤ 1.4 km s^{-1} and explains the small observed rise velocity of emerging flux in the photosphere. The numerical results also show strong downdrafts with $\sim$1–3 km s^{-1} at the early stage of magnetic flux expansion, which may correspond to observed strong downdrafts near pores.

4. Strong MHD shock waves are formed near the footpoint of the loop by the downflow along the loop when the loop reaches a height of about $10H \simeq 2000$ km. Both fast and intermediate MHD shocks are shown to occur.

5. Kinetic energy flux carried by the downflow along the loop, which is converted into thermal (internal) energy by

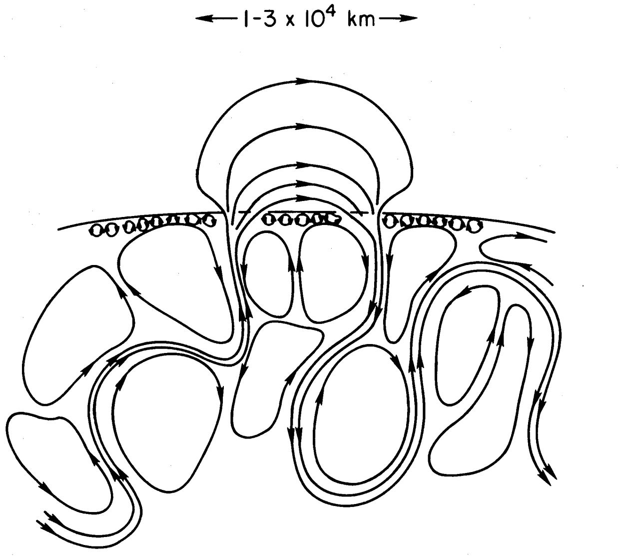

FIG. 12.—Hypothetical magnetic field configuration in the solar convection zone just below an emerging flux region.

shock waves near the footpoint of the loop, amounts to 6×10^6 ergs cm^{-2} s^{-1}. This explains a part of the chromospheric heating in bright plages in EFRs.

6. The magnetic energy stored in the initial magnetic flux in or below the photosphere is substantially released by the expansion of magnetic flux. The released magnetic energy is comparable to the released gravitational energy, and both energies are finally converted into thermal (internal) energy through compressional and shock heating. The release rate of magnetic energy is $\sim 4 \times 10^9$ ergs cm^{-2} s^{-1}, and is sufficient to explain enhanced activities in EFRs.

7. When there is an overlying coronal magnetic field, which is parallel to the emerging field, the expansion of the magnetic loop is significantly decelerated. However, for an antiparallel coronal field, the expansion of the loop is *not* decelerated, because of magnetic reconnection. This reconnection is similar to the dayside reconnection in terrestrial magnetospheres, and a jet-type flow is produced by the gas pressure gradient along the reconnected field line, because the gas pressure in the corona is larger than that in the emerging flux. This jet-type flow may correspond to small surges sometimes observed in EFRs.

Previous numerical studies of flux emergence also showed the development of downflows along the legs of the magnetic loop. In the work by Nakagawa, Steinolfson, and Wu (1976), the downflow resulted when the expanding magnetic loop compressed ambient coronal material that was then forced to flow downward along the field lines. Although they included the effect of gravity, the dominant force to produce the downflow was not gravity. Forbes and Priest (1984) examined flux emergence into an antiparallel ambient field without gravity, and the downflow was produced because of reconnection. A new aspect of our model is that the main force to accelerate the downflow along the loop is gravity.

Finally, we should note that the actual process of magnetic flux emergence is a three-dimensional process. The three-dimensional effect is important in the convection zone (and probably in the photosphere) to create an isolated flux tube by the interchange instability. According to the preliminary study of the nonlinear evolution of the interchange mode of magnetic buoyancy instability (Shibata, Tajima, and Matsumoto 1989), the nonlinear rise speed of the magnetic flux for the pure interchange instability is much smaller than that for the pure undular instability. This means that the actual rise speed of the loop is determined by the nonlinear dynamics of the undular instability. Thus, the physical theory as well as the quantitative results in this paper may not be significantly altered by considering the interchange processes.

Here, we comment on the origin of the "filamentary structure" observed in AFSs. In the photosphere and the convection zone, it is likely that the magnetic flux tube is embedded in a field-free medium (high-β medium), and so the interchange instability is one of the primary mechanisms for the filamentary structure observed in the photosphere, such as the granular dark lanes. However, in the upper chromosphere and the corona, even if there is no magnetic field initially, the emerging magnetic fields expand to cover the whole space as shown in the numerical results of this paper, as long as the magnetic pressure in the loop is larger than the gas pressure in the corona. Thus, observed filamentary structures in AFS filaments do not suggest the presence of isolated magnetic filaments in a field-free medium, but suggest that the density (and/or the temperature) may have filamentary structure. In fact, our simulation results show the high-density loop (filament) at the top of the expanding magnetic flux. The density enhancement is even larger when a neutral sheet is created between the emerging flux and the coronal field. It is also possible that the filamentary (density) structure may be created by the pinch effect due to the helical magnetic twist in a three-dimensional process.

There are other important three-dimensional effects produced by magnetic shear and the helical magnetic twist. The former can be partly studied by the 2.5-dimensional numerical simulation and will be discussed in a separate paper (Shibata, Tajima, and Matsumoto 1989). The latter leads to an intrinsically three-dimensional process such as the kink instability (Sakurai 1976; Zaidman and Tajima 1989) and must be studied by a fully three-dimensional MHD numerical simulation. The coupling between the undular and the kink instabilities may produce a larger rise velocity of the loop than that found in this paper. Furthermore, this process may be interesting in relation to the flare as discussed by Piddington (1975, 1976*a*, *b*), Parker (1974), Tanaka (1987), and Kurokawa (1988*b*). These problems will be studied in our future three-dimensional MHD simulations.

The authors thank E. N. Parker, R. Rosner, H. Zirin, Y. Uchida, H. Kurokawa, Y. Suematsu, and D. Chou for useful discussions. They also thank J. Schutkeker for his kind help in using the computers and graphics software. Computations were performed on the Cray X-MP/24 at the Computer Center of the University of Texas at Austin. This work was supported in part by the National Science Foundation grant ATM85-06646, NASA grant NAG W-846, and US Department of Energy DE-FG05-80ET53088. R. S. Steinolfson was supported in part by a NASA *SMM* Guest Investigator Grant.

REFERENCES

Born, R. 1974, *Solar Phys.*, **38**, 127.
Brants, J. J. 1985, *Solar Phys.*, **98**, 197.
Brants, J. J., and Steenbeck, J. C. M. 1985, *Solar Phys.*, **96**, 229.
Bray, R. J., and Loughhead, R. E. 1964, *Sunspots* (London: Chapman & Hall).
Brunel, F., Tajima, T., and Dawson, J. M. 1982, *Phys. Rev. Letters*, **49**, 323.
Bruzek, A. 1967, *Solar Phys.*, **2**, 451.
———. 1969, *Solar Phys.*, **8**, 29.
Bumba, J. 1967, in *Plasma Astrophysics*, ed. P. A. Sturrock (New York: Academic), p. 77.
Bumba, V., and Howard, R. 1965, *Ap. J.*, **141**, 1492.
Canfield, R. C., and Fisher, R. R. 1976, *Ap. J.* (*Letters*), **210**, L149.
Chou, D., and Fisher, G. H. 1989, *Ap. J.*, **341**, 533.
Chou, D., and Wang, H. 1987, *Solar Phys.*, **110**, 81.
Chou, D., and Zirin, H. 1988, *Ap. J.*, **333**, 420.
Choudhuri, A. R., and Gilman, P. A. 1987, *Ap. J.*, **316**, 788.
Fisher, G. H., Chou, D., and McClymont, A. N. 1988, preprint.
Forbes, T. G., and Priest, E. R. 1984, *Solar Phys.*, **94**, 315.
Frazier, E. N. 1972, *Solar Phys.*, **26**, 130.
Glackin, D. L. 1975, *Solar Phys.*, **43**, 317.
Golub, L., Krieger, A. S., Harvey, J. W., and Vaiana, G. S. 1977, *Solar Phys.*, **53**, 111.
Golub, L., Krieger, A. S., and Vaiana, G. S. 1976, *Solar Phys.*, **49**, 79.
Golub, L., Rosner, R., Vaiana, G. S., and Weiss, N. O. 1981, *Ap. J.*, **243**, 309.
Harvey, K. L., Harvey, J. W., and Martin, S. F. 1975, *Solar Phys.*, **40**, 87.
Harvey, K. L., and Martin, S. F. 1973, *Solar Phys.*, **32**, 389.
Heyvaerts, J., Priest, E. R., and Rust, D. M. 1977, *Ap. J.*, **216**, 123.
Horiuchi, T., Matsumoto, R., Hanawa, T., and Shibata, K. 1988, *Pub. Astr. Soc. Japan*, **40**, 147.
Hoshino, M., and Nishida, A. 1983, *J. Geophys. Res.*, **88**, 6926.
Hughes, D. W., and Cattaneo, F. 1987, *Geophys. Ap. Fluid Dyn.*, **39**, 65.
Kantrowitz, A. R., and Petschek, H. E. 1966, in *Plasma Physics in Theory and Application*, ed. W. B. Kunkel (New York: McGraw-Hill), p. 147.

Kawaguchi, I., and Kitai, R. 1976, *Solar Phys.*, **46**, 125.
Kundu, R., and Woodgate B. (eds.). 1986, *Proc. SMM Workshop on Energetic Phenomena on the Sun* (NASA CP-2439), chap. 1.
Kurokawa, H. 1988*a*, in *Proc. Fourth Asian-Pacific Regional Meeting of the IAU* (*Vistas Astr.*, **31**, 67).
———. 1988*b*, *Solar Phys.*, **113**, 259.
Leboeuf, J. N., Tajima, T., Kennel, C. F., and Dawson, J. M. 1978, *Geophys. Res. Letters*, **5**, 609.
Marsh, K. A. 1978, *Solar Phys.*, **59**, 105.
Matsumoto, R., Horiuchi, T., Shibata, K., and Hanawa, T. 1988, *Pub. Astr. Soc. Japan*, **40**, 171.
Meyer, F., Schmidt, H. U., Simon, G. W., and Weiss, N. O. 1979, *Astr. Ap.*, **76**, 35.
Moreno-Insertis, F. 1986, *Astr. Ap.*, **166**, 291.
Nakagawa, Y., Steinolfson, R. S., and Wu, S. T. 1976, *Solar Phys.*, **47**, 193.
Parker, E. N. 1955, *Ap. J.*, **122**, 293.
———. 1966, *Ap. J.*, **145**, 811.
———. 1974, *Ap. J.*, **191**, 245.
———. 1979, *Cosmical Magnetic Fields* (Oxford: Clarendon Press).
———. 1987, *Ap. J.*, **312**, 868.
———. 1988, *Ap. J.*, **326**, 407.
Petschek, H. E. 1964, in *Proc. AAS–NASA Symposium on Physics of Solar Flares* (NASA SP-50), p. 425.
Piddington, J. H. 1975, *Ap. Space Sci.*, **34**, 347.
———. 1976*a*, *Ap. Space Sci.*, **41**, 79.
———. 1976*b*, *Ap. Space Sci.*, **45**, 47.
Priest, E. R. 1982, *Solar Magnetohydrodynamics* (Dordrecht: Reidel).
Richtmyer, R. O., and Morton, K. W. 1967, *Difference Methods for Initial-Value Problems* (2d ed.; New York: Interscience), chap. 13.
Rubin, E., and Burstein, S. Z. 1967, *J. Comput. Phys.*, **2**, 178.
Rust, D. M. 1972, *Solar Phys.*, **25**, 141.
Sakurai, T. 1976, *Pub. Astr. Soc. Japan*, **28**, 177.
Sato, T., and Hayashi, T. 1979, *Phys. Fluids*, **22**, 1189.
Schüssler, M. 1977, *Astr. Ap.*, **56**, 439.
———. 1979, *Astr. Ap.*, **71**, 79.
———. 1980, *Astr. Ap.*, **89**, 26.
Sheeley, N. R., and Golub, L. 1979, *Solar Phys.*, **63**, 119.
Shibata, K. 1980, *Solar Phys.*, **66**, 61.
Shibata, K., and Suematsu, Y. 1982, *Solar Phys.*, **78**, 333.
Shibata, K., Tajima, T., and Matsumoto, R. 1989, in preparation.
Shibata, K., Tajima, T., Matsumoto, R., Horiuchi, T., Hanawa, T., Rosner, R., and Uchida, Y. 1989, *Ap. J.*, **338**, 471.
Soward, A. M., and Priest, E. R. 1986, *J. Plasma Phys.*, **35**, 333.
Steinolfson, R. S., and Hundhausen, A. J. 1988, *J. Geophys. Res.*, submitted.
Suematsu, Y. 1987, private communication.
Svestka, Z. 1976, *Solar Flares* (Dordrecht: Reidel).
Tajima, T., Sakai, J., Nakajima, H., Kosugi, T., Brunel, F., and Kundu, M. R. 1987, *Ap. J.*, **321**, 1031.
Tanaka, K. 1987, *Pub. Astr. Soc. Japan*, **39**, 1.
Tarbel, T., Ferguson, S., Frank, Z., Title, A., and Topka, K. 1988, *Bull. AAS*, **20**, 680.
Tsinganos, K. 1980, *Ap. J.*, **239**, 746.
Tsuda, T., and Ugai, M. 1977, *J. Plasma Phys.*, **18**, 451.
Uchida, Y., and Sakurai, T. 1977, *Solar Phys.*, **51**, 413.
Uchida, Y., and Shibata, K. 1988, *Solar Phys.*, **116**, 291.
Ugai, M., and Tsuda, T. 1977, *J. Plasma Phys.*, **17**, 337.
Weart, S. R. 1970, *Ap. J.*, **162**, 987.
Zaidman, E. G., and Tajima, T. 1989, *Ap. J.*, **338**, 1139.
Zirin, H. 1970, *Solar Phys.*, **14**, 328.
———. 1972, *Solar Phys.*, **22**, 34.
———. 1974, in *IAU Symposium 56, Chromospheric Fine Structure*, ed. R. G. Athay (Dordrecht: Reidel), p. 161.
Zirin, H., and Tanaka, K. 1973, *Solar Phys.*, **32**, 173.
Zwaan, C. 1985, *Solar Phys.*, **100**, 397.
———. 1987, *Ann. Rev. Astr. Ap.*, **25**, 83.

RYOJI MATSUMOTO: Department of Information Science, College of Arts and Sciences, Chiba University, Yayoi-cho, Chiba 260, Japan

KAZUNARI SHIBATA: Department of Earth Sciences, Aichi University of Education, Kariya, Aichi 448, Japan

RICHARD S. STEINOLFSON and TOSHIKI TAJIMA: Department of Physics and Institute for Fusion Studies, University of Texas at Austin, Austin, TX 78712